

Machine Learning Green's Functions of Strongly Correlated Hubbard Models

Mateo Cárdenes Wuttig*

*Department of Chemistry, Yale University, New Haven, Connecticut 06520, United States and
Department of Applied Physics, Yale University, New Haven, Connecticut 06520, United States*

(Dated: November 11, 2025)

We demonstrate that a machine learning framework based on kernel ridge regression can encode and predict the self-energy of one-dimensional Hubbard models using only mean-field features such as static and dynamic Hartree-Fock quantities and first-order GW calculations. This approach is applicable across a wide range of on-site Coulomb interaction strengths U/t , ranging from weakly interacting systems ($U/t \ll 1$) to strong correlations ($U/t > 8$). The predicted self-energy is transformed via Dyson's equation and analytic continuation to obtain the real-frequency Green's function, which allows access to the spectral function and density of states. This method can be used for nearest-neighbor interactions t and long-range hopping terms t' , t'' , and t''' .

I. INTRODUCTION

In this article, we extend a previously introduced machine learning (ML) framework developed for molecules[1] to strongly correlated electronic systems, characterized by suppressed quasi-particle peaks, large self-energy, and broad bands[2–5]. For weakly interacting systems, one can obtain an accurate mean-field solution through Hartree-Fock (HF) calculations, where the quantum many-body wavefunction is approximated as a single Slater determinant[6, 7], neglecting quantum fluctuations. Density-functional theory (DFT) enables accurate and efficient computations based on the electron density[8], although the exact energy functional remains unknown, and approximate exchange–correlation functionals lead to systematic errors[9]. Spectral properties of systems where electron correlations must be considered explicitly, however, require numerically intensive many-body methods that are typically limited to small or low-dimensional systems[10–12], such as many-body perturbation theory (GW)[13] or coupled-cluster (CC) theory[14, 15]

Here, we demonstrate an ML model that learns the imaginary-frequency self-energy function from mean-field input features and generalizes to previously unseen model parameters, providing many-body spectral predictions based on mean-field data. We study the one-dimensional half-filled Hubbard model with varying on-site repulsion U . This system is well-understood[16–18], making it an ideal candidate to investigate the quality of ML predictions. We use the many-body Green's function formalism[19] to calculate spectral properties[20]. A large variety of methods, such as GW or CC, can be expressed in this framework, which may allow our ML architecture to be used as a bridge between mean-field calculations at the HF level and approximate many-body approaches.

We note that a large number of ML approaches have been used to simulate correlated quantum systems. However, many methods, such as restricted Boltzmann machines[21, 22], deep neural networks[23], and Transformer architectures[24], commonly described as Neural Quantum States (NQS)[25], are not well-suited to describe excited states. Additionally, they often require large training datasets or only achieve accurate results for specific parameter values or optimization schemes[26]. Calculating spectral properties based on ML methods remains challenging[20], even with state-of-the-art architectures[21, 27–30]. On the other hand, there exists a large variety of methods that can find highly accurate descriptions of many-body ground states, including tensor networks[31, 32], Quantum Monte Carlo[33], and NQS[34–36]. These methods, however, do not allow for a precise computation of spectral quantities. Additionally, some methods, such as tensor networks, are particularly well-suited for (quasi) one-dimensional systems[37] and struggle with long-range interactions[38] or periodic boundary conditions[39], while others, like Quantum Monte Carlo, suffer from the sign problem with increasing Coulomb repulsion[40].

Our approach consists of using a Kernel Ridge Regression (KRR) architecture[41] to learn and predict the self-energy on a compact imaginary frequency grid. We can combine this quantity with the mean-field Green's function via Dyson's equation to obtain the many-body Green's function. The real-frequency spectral quantities, such as the spectral function and density of states, can be obtained via analytic continuation from the functions calculated on the imaginary axis[42].

This work provides a route to ML-based methods that may offer several advantages in comparison to existing numerical methods. First, our method is accurate for short-range nearest-neighbor interactions as well as long-range hoppings. Additionally, there is no structural difference between open and periodic boundary conditions, and the framework maintains consistent ac-

* mateo.cardeneswuttig@yale.edu

curacy even for long-range interactions. We investigate different hopping parameters t, t', t'' and t''' between up to four neighbors, all of which are realized in different condensed matter systems, making our method a versatile approach for the study of spectral properties in real materials. Lastly, our method works well over a broad range of interaction strengths U/t from weak to strong correlations. In addition, the KRR model is fully interpretable, increasing confidence in the results, which makes it stand out compared to most other ML architectures. This is of major advantage in understanding how mean-field quantities are related to many-body correlations.

The article is structured as follows. In section II, we introduce the ML architecture and workflow and explain our metric of accuracy. In section III A, we demonstrate that our ML framework can encode the self-energy of a nearest-neighbor Hubbard model for a wide range of Coulomb repulsions U , reproducing the training data and generalizing to unseen test data. We argue that the differences between the exact density of states and the ML prediction mainly stem from the analytic continuation. To prove this, we present an extensive overview of the absolute relative difference between the predicted and exact self-energy. Then, we show in section III B that our ML model also allows for accurate predictions of systems with long-range hopping terms $t', t'',$ and t''' . In section IV, we discuss our results.

II. METHODS

A. 1d Hubbard Model

We consider a one-dimensional Hubbard model of length $L = 10$ with periodic boundary conditions at half-filling, described by the following Hamiltonian

$$H = - \sum_{\langle ij \rangle, \sigma} t_{ij} (c_{i\sigma}^\dagger c_{j\sigma} + \text{h.c.}) + U \sum_i n_{i\uparrow} n_{i\downarrow} \quad (1)$$

where $c_{i\sigma}^\dagger$ ($c_{i\sigma}$) creates (destroys) an electron of spin $\sigma = \uparrow, \downarrow$ on site $i = 1, \dots, L$, and $n_{i\sigma} = c_{i\sigma}^\dagger c_{i\sigma}$ counts the number of electrons. We sum over all bonds $\langle ij \rangle$ and consider nearest-neighbor interactions $t_{ij} = t$ for $|i - j| = 1$ and long-range interactions $t_{ij} = t^{(n)} \delta_{|i-j|, n}$ between two ($t' = t^{(2)}$), three ($t'' = t^{(3)}$), and four ($t''' = t^{(4)}$) neighbors. In fig. 1, we present these systems, including a Hubbard chain with nearest neighbor interactions t (a); next-nearest neighbor hopping t' (b), which resembles a zig-zag ladder; next-next-nearest neighbor hopping t'' (c), equivalent to a zig-zag ladder with diagonal interactions; and also a t''' -hopping (d), corresponding to a folded zig-zag ladder with an arm-chair structure, where t''' describes hopping between

two layers of zig-zag ladders. All parameters are given in units of $t = 1$.

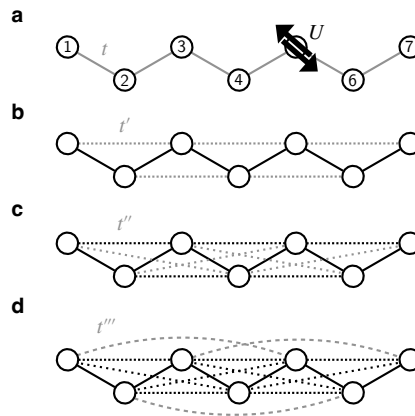


FIG. 1. One-dimensional Hubbard model with on-site Coulomb repulsion U . (a) Nearest-neighbor hopping t . (b) Zig-zag ladder with next-neighbor hopping t' . (c) Zig-zag ladder with diagonal hopping term t'' . (d) Additional hopping t''' between next-nearest-neighbor atoms on both legs of the zig-zag ladder.

B. Many-Body Green's Function

The single-particle Green's function describes how an electron propagates from site j at time $t_0 = 0$ to site i at time $t > 0$

$$G(t)_{ij}^\sigma = -i\theta(t) \langle \psi_0 | c_{i\sigma}(t) c_{j\sigma}^\dagger(t_0) | \psi_0 \rangle. \quad (2)$$

Here, $|\psi_0\rangle$ denotes the ground state wave function at zero temperature. We only consider the retarded Green's function, and we fix $\sigma = \uparrow$ and omit the spin index. In the frequency domain, the addition part of the Green's function is defined as

$$G(z)_{ij}^{\text{EA}} = \langle \psi_0 | c_{i\sigma} \frac{1}{z - (\hat{H} - E)} c_{j\sigma}^\dagger | \psi_0 \rangle \quad (3)$$

such that $G(z) = G(z)^{\text{EA}} + G(z)^{\text{IP}}$ is the sum of the removal (IP) and addition (EA) parts. E is the ground state energy determined by the Hamiltonian \hat{H} . We can express the propagator both on the real frequency axis $z = \omega + i\eta$ as a function of energy with a broadening factor η , or on the imaginary frequency axis $z = E_F + i\omega$, where E_F is the Fermi energy. We know that $E_F = U/2$ at half-filling for the nearest-neighbor Hubbard model, and we present the density of states (DOS) as a function of $E - U/2$. We use a discrete set of $N_{\omega_k} = 30$ imaginary frequencies $\{i\omega_k\}$ with $k = 1, \dots, N_{\omega_k}$ based on a modified Gauss-Legendre grid[1] to describe the

Green's function. Hence, $G(\omega)$ is a set of N_{ω_k} matrices of shape $N_{AO} \times N_{AO}$, where the number of atomic orbitals is $N_{AO} = L$.

We can relate the non-interacting mean-field Green's function G_0 , obtained from Hartree-Fock (HF) calculations, and the self-energy Σ to the many-body Green's function G via Dyson's equation:

$$G^{-1}(\omega) = G_0^{-1}(\omega) - \Sigma(\omega). \quad (4)$$

Thus, we only have to know one of (G, Σ) to obtain the many-body spectral properties for a given G_0 . Note that all three objects have the same shape $N_{\omega_k} \times N_{AO} \times N_{AO}$, where eq. 4 is a matrix equation. The many-body Green's function G on the real axis gives access to the spectral function

$$A(\omega) = -\frac{\text{Im}[G(\omega)]}{\pi} \quad (5)$$

and the density of states

$$\text{DOS}(\omega) = \text{Tr}[A(\omega)]. \quad (6)$$

In our workflow, we predict the self-energy on a discrete imaginary frequency axis $\Sigma(\{i\omega_k\})$ since this function is smooth and thus an easier target for the ML model[1]. We use Padé analytic continuation[43] to transform the self-energy from the imaginary frequency axis to the real energy axis $\Sigma(\{i\omega_k\}) \rightarrow \Sigma(\{E_k\} - U/2)$ with a broadening factor of $\eta = 0.015$. We use a linear grid of 400 energy points $\{E_k\} \in [-2, 2]$ eV for $U/t < 4$, $\{E_k\} \in [-6, 6]$ eV for $U/t < 8$, and $\{E_k\} \in [-10, 10]$ eV otherwise. All HF calculations are performed with an iterative algorithm that gradually introduces random noise to the initial guess of the density matrix until the calculation converges. The converged Restricted Hartree-Fock (RHF) state is used to calculate G_0 . The exact Green's function G is computed via Full-Configuration Interaction (FCI). All calculations are performed at zero temperature. Both G and G_0 are computed in molecular orbital (M.O.) basis and are transformed to atomic orbital (A.O.) basis. We perform all ML predictions in A.O. basis to benefit from the translation invariance symmetry of the Hamiltonian. We use the PySCF package[44, 45] and the FCDMFT package[12, 46, 47] for Green's function and GW calculations[48].

C. Machine-Learning Workflow

In the following, we refer to the exact many-body Green's function computed by FCI as FCI-GF, to the mean-field Green's function computed by RHF as HF-GF, and to the predicted Green's function as ML-GF. Our workflow is based on a previous work by Venturella

et al.[1] For each Hamiltonian defined by the hopping parameters (t, t', t'', t''') , we define separate KRR models f for on- and off-diagonal elements as well as the real and imaginary parts of every frequency value ω_k . These $4N_{\omega_k}$ independent models are trained with data for different values of U . For all calculations, we provide 604 FCI-GF as training data and 21 FCI-GF as test data with mutually exclusive Coulomb repulsion values between $U = 0.25$ and $U = 10$. Our ML model $f^{\text{on/off,Re/Im},\omega_k}$ learns by using the self-energy $\Sigma(\omega_k)_{ij}^{\text{training}}$, obtained from the FCI-GF training data via eq. 4, as a target with features $\mathbf{f}_{ij}^{\text{training}}$

$$f^{\text{on/off,Re/Im},\omega_k}(\mathbf{f}_{ij}^{\text{training}}) \rightarrow \text{Re/Im}[\Sigma(\omega_k)_{ij}^{\text{training}}]. \quad (7)$$

Once trained, the model can predict a self-energy based on features of unseen test data $\mathbf{f}_{ij}^{\text{test}}$

$$\text{Re/Im}[\Sigma(\omega_k)_{ij}^{\text{pred}}] = f^{\text{on/off,Re/Im},\omega_k}(\mathbf{f}_{ij}^{\text{test}}) \quad (8)$$

which can be converted to the ML-GF G^{pred} via Dyson's equation by combining $\Sigma^{\text{pred}} = \text{Re}(\Sigma^{\text{pred}}) + i \text{Im}(\Sigma^{\text{pred}})$ with G_0 . The feature vector \mathbf{f}_{ij} is independent of frequency ω_k and contains the following 54 elements

$$\begin{aligned} \mathbf{f}_{ij} = & \left(U, h_{ij}, F_{ij}, J_{ij}, K_{ij}, \rho_{ij}, \right. \\ & \left. \{\text{Re}[G_0(\omega_n)_{ij}]\}_{n=1,\dots,2N_{\omega_n}}, \{\text{Im}[G_0(\omega_n)_{ij}]\}, \right. \\ & \left. \{\text{Re}[\Delta(\omega_n)_{ij}]\}_{n=1,\dots,N_{\omega_n}}, \{\text{Im}[\Delta(\omega_n)_{ij}]\}, \right. \\ & \left. \{\text{Re}[\Sigma_{\text{GW}}(\omega_n)_{ij}]\}, \{\text{Im}[\Sigma_{\text{GW}}(\omega_n)_{ij}]\} \right). \end{aligned} \quad (9)$$

We include the on-site repulsion U and the matrix elements (i, j) of the core Hamiltonian matrix h , the Fock matrix F , the Coulomb matrix J , the exchange matrix K , and the one-electron reduced density matrix ρ . Additionally, we provide the respective real and imaginary matrix elements of the HF-GF $G_0(\omega_n)$ for $2N_{\omega_n}$ different imaginary frequencies from a modified Gauss-Legendre grid, where $N_{\omega_n} = 6$, and the hybridization function $\Delta(\omega_n)$, defined separately for on- and off-diagonal elements

$$\begin{aligned} \Delta(\omega)_{ij} = & E_F + i\omega - F_{ij} + \\ & \begin{cases} (G_0(\omega)^{-1})_{ii}, & i = j \\ \frac{G_0(\omega)_{ij}}{G_0(\omega)_{ij}G_0(\omega)_{ji} - G_0(\omega)_{ii}G_0(\omega)_{jj}}, & i \neq j \end{cases} \end{aligned} \quad (10)$$

where E_F is determined from HF calculations. We also include a first order G_0W_0 calculation for the self-energy $\Sigma_{\text{GW}}(\omega_n)$. Note that $\Delta(\omega_n)$ and $\Sigma_{\text{GW}}(\omega_n)$ are computed for N_{ω_n} imaginary frequency values. All features are transformed from M.O. to A.O. basis. We use a min-max normalization and log-scaling on all feature vectors to enhance the predictive quality by ensuring that the features are distributed evenly. The predicted

self-energy is symmetrized with respect to the diagonal axis.

For a given feature vector $\tilde{\mathbf{f}}$, our KRR model $f^m = f^{\text{on/off,Re/Im},\omega_k}$ predicts:

$$f^m(\tilde{\mathbf{f}}) = \sum_{n=1}^N \alpha_n^m K(\tilde{\mathbf{f}}, \mathbf{f}_n), \quad (11)$$

where K is the kernel function. We use a superposition of three (K_3) Matérn covariance functions:

$$K_3 = 1 + M_1 + 0.5M_{0.5} + 0.25M_{0.1} \quad (12)$$

or, if mentioned, six (K_6) kernel functions:

$$K_6 = K_3 + 0.4M_{0.35} + 0.33M_{0.25} + 0.1M_{0.05}. \quad (13)$$

The individual Matérn kernels $M_l = M_l(\mathbf{x}, \mathbf{y})$ are defined as

$$M_l(\mathbf{x}, \mathbf{y}) = \frac{1}{\Gamma(\nu)2^{\nu-1}} \left(\frac{\sqrt{2\nu}}{l} \|\mathbf{x}, \mathbf{y}\| \right)^\nu I_\nu \left(\frac{\sqrt{2\nu}}{l} \|\mathbf{x}, \mathbf{y}\| \right). \quad (14)$$

where $\|\mathbf{x}, \mathbf{y}\|$ is the Euclidean distance between two vectors \mathbf{x} and \mathbf{y} , l is the length scale, $\Gamma(\nu)$ is the Gamma function, and $I_\nu(z)$ is the modified Bessel function[49]. We always use $\nu = 1.5$ and only vary l [50]. The prediction in eq. 11 depends on the distance defined by K between our input feature vector $\tilde{\mathbf{f}}$ and the feature vector of the training data \mathbf{f}_n for $n = 1, \dots, N$, where $N = N_d \cdot N_{\text{on/off}}$ denotes the number of training data points, which depend on the number of on/off-diagonal elements $N_{\text{on/off}}$ and the number of FCI-GF provided for training N_d . The regression coefficients $\boldsymbol{\alpha}^m = [\alpha_1^m, \dots, \alpha_N^m]^T$ are determined by inverting the kernel matrix \mathbf{K} with a small regularization parameter $\lambda = 10^{-4}$:

$$\boldsymbol{\alpha}^m = (\mathbf{K} + \lambda \mathbf{1})^{-1} \mathbf{t}^m \quad (15)$$

where \mathbf{t}^m is a vector of self-energy targets from the training data, see eq. 7, and \mathbf{K} is defined by its entries $\mathbf{K}_{nm} = K(\mathbf{f}_n, \mathbf{f}_m)$. This is equivalent to the following loss function

$$\mathcal{L}(\boldsymbol{\alpha}^m) = \|\mathbf{K}\boldsymbol{\alpha}^m - \mathbf{t}^m\|^2 + \lambda(\boldsymbol{\alpha}^m)^T \mathbf{K}\boldsymbol{\alpha}^m, \quad (16)$$

which depends on the residuals between predictions $\mathbf{K}\boldsymbol{\alpha}^m$ and targets \mathbf{t}^m [51]. We use scikit-learn in Python for the ML workflow[50].

D. Metrics of Accuracy

We use the absolute relative difference (ARD)[20] between the self-energy prediction Σ^{pred} and the exact solution Σ^{exact} to evaluate the accuracy of our ML model.

This metric represents a percentage deviation from the exact result. The ARD can be defined as a function of U -values in the test or training data

$$\text{ARD}(U)|_{\text{on,off}} = \frac{1}{N_{\text{on/off}}} \sum_{i,j=1}^L \sum_{k=1}^{N_{\omega_k}} \frac{|\Sigma_{i,j,k}^{\text{pred}} - \Sigma_{i,j,k}^{\text{exact}}|}{|\Sigma_{i,j,k}^{\text{exact}}|} \quad (17)$$

which we calculate separately for all $N_{\text{on}} = L$ on-diagonal ($i = j$) and $N_{\text{off}} = L^2 - L$ off-diagonal ($i \neq j$) matrix elements, respectively, as an average over all frequencies $k = 1, \dots, N_{\omega_k}$. Another quantity of interest is the ARD as an average over all matrix elements for a fixed frequency:

$$\text{ARD}(U)|_{\omega_n} = \frac{1}{N_{\text{on}} + N_{\text{off}}} \sum_{i,j} \frac{|\Sigma_{i,j,k}^{\text{pred}} - \Sigma_{i,j,k}^{\text{exact}}|}{|\Sigma_{i,j,k}^{\text{exact}}|}. \quad (18)$$

Similarly, we can define the absolute relative difference as a function of imaginary frequencies $\text{ARD}(\omega_n)$ for all on- and off-diagonal elements ($\text{ARD}(\omega_n)|_{\text{on,off}}$) and for all U -values ($\text{ARD}(\omega_n)|_U$).

III. RESULTS

A. Nearest-Neighbor Interactions

1. Test Data

First, we investigate the predictive power of our ML framework in the case of nearest-neighbor interactions. In fig. 2(a)-(c), we present the local self-energy $\Sigma_{i,i}$ on the first site $i = 1$ as a function of imaginary frequencies for different Coulomb interaction strengths $U = 1$, $U = 2$, and $U = 8$, respectively. All of these values correspond to test data not used during training. We observe indistinguishable curves for the predictions (ML, orange, small circles) in comparison to the exact function (FCI, blue, large circles), both for the imaginary part (dashed lines) and the near-zero real part (solid lines). In fig. 2(d)-(f), we compare the exact density of states (DOS) obtained from FCI and the ML prediction for the same U -values presented in the top row. The ML model predicts the energies of all peaks and the approximate shape and height correctly, although the precision is reduced further away from the Fermi edge. The predicted DOS matches the exact DOS better when the system is weakly correlated, compare, e.g., fig. 2(d) to (f). However, it is important to note that the DOS is plotted over a larger range of energies to show the full electronic structure.

In the following, we present both on the DOS and the self-energy, but it is important to note that our

ML model only predicts the Green's function on the imaginary axis, while the DOS is obtained via analytic continuation (A.C.), which introduces additional errors. The FCI-GF is computed on the imaginary axis, ensuring that the self-energy target is exact. This is also a computationally less expensive way of obtaining large amounts of training data. However, the true FCI-GF computed directly on real frequencies may deviate from the reference function to which we compare our ML predictions. Hence, one may not accurately assess the quality of this model by evaluating the DOS, which is why we use the absolute relative difference (ARD) of the self-energy, see eq. 17 and 18, to estimate the accuracy of our ML model. We argue that the main source of error in the predicted DOS originates from the A.C. when transforming the Green's function to the real axis, not from the quality of the ML predictions on the imaginary axis. To support this, we compare the results for test data to the DOS for training data, and we present a comprehensive overview of the ARD.

2. Training Data

In fig. 3(a)-(c), we show the local self-energy on the first site for training data with $U = 1.0625$, $U = 2.046875$, and $U = 8.109375$, respectively. This data is presented in normalized units to visualize the excellent agreement between the ML prediction and the exact solution. Similar to the previous results, we observe that the ML model accurately reproduces the peak shapes and heights in the DOS, see fig. 3(d)-(f). We observe similar deviations between the predicted DOS and the exact result when comparing test data in fig. 2(f) and training data in fig. 3(f). This supports our claim that the main source of deviations stems from the A.C. method, which becomes clear when we compare the self-energy ARD between test and training data.

3. Accuracy of Predictions

The absolute relative difference (ARD) between exact and predicted self-energy for test data from fig. 2 is presented in fig. 4(a)-(d). Figure 4(a) shows the ARD for on-diagonal (purple) and off-diagonal (yellow) matrix elements over all frequencies as a function of Coulomb repulsion U , see eq. 17. The colored areas correspond to the standard deviation. The predictions have the lowest error for small and intermediate U -values, with relative differences between 10^{-5} and 10^{-4} . In contrast, systems with stronger correlations ($U > 8$) can be predicted less accurately, leading to a relative error of up to 10%. Interestingly, there is a large range of Coulomb repulsions up to $U \approx 6$ that can be predicted

with the same relative error. This raises the question of whether the increased error at large U arises from complex excitation properties that are difficult to capture with mean-field data, and whether it can be mitigated by including training samples at even larger Coulomb interactions. Figure 4(b) shows the same trends as fig. 4(a), but visualized for different imaginary frequencies. We use an adapted Gauss-Legendre grid, meaning that the mapping of frequency index to frequency value is not linear (see fig. 2(d)-(f)), where ω_1 (purple) represents the smallest frequency value, and ω_{30} (yellow) the largest value. The smallest frequency values can be predicted less accurately due to the more complicated low-energy physics near the Fermi edge. Each data point in fig. 4(c) stems from an independent ML model, see eq. 18, which shows that our ML architecture is well-suited to learn the self-energy over a broad range of frequencies. Similar to fig. 4(b), we observe that the self-energy of the largest frequency values can be predicted with accuracies as low as 10^{-4} , while the relative error increases for smaller frequencies. In fig. 4(d), we present the ARD over all matrix elements for different U -values as a function of frequency. We find that the best predictions can be achieved for small and intermediate U -values, but not for the smallest value $U = 0.25$. This is most likely due to the fact that we did not provide training data for $U < 0.25$.

We present the same overview of the ARD for our training data in fig. 4(e)-(h). Similar to test data, we find that the ARD is lowest for small and intermediate U -values up to $U \approx 6$, see fig. 4(e), while the relative error increases with larger U -values. The on-diagonal elements are predicted with an ARD of 10^{-4} even for the largest U -values, while we find relative errors as low as 10^{-6} for smaller U -values. Note that the diagonal elements of the self-energy are more important for the predictions than the off-diagonal ones. We observe lower relative errors for training data compared to test data, compare fig. 4(f) to (b), respectively. This increases our confidence in the model's ability to memorize the training data, meaning that the mean-field features are sufficient for our KRR model to reproduce many-body spectral quantities. In the appendix, we show that we are not providing the self-energy target by including a first-order G_0W_0 calculation in the feature vector[52]. The observation that both fig. 4(e) and (g) have similar shapes when comparing on- versus off-diagonal elements over different U -values or frequencies, respectively, shows that our ML model is a sensible approach to learn the full self-energy function, including on-diagonal elements representing local interaction corrections and off-diagonal non-local correlation effects between different sites. This can also be inferred from the relatively constant ARD over a large range of frequencies in fig. 4(g) and (h).

For models with nearest-neighbor hopping, the DOS

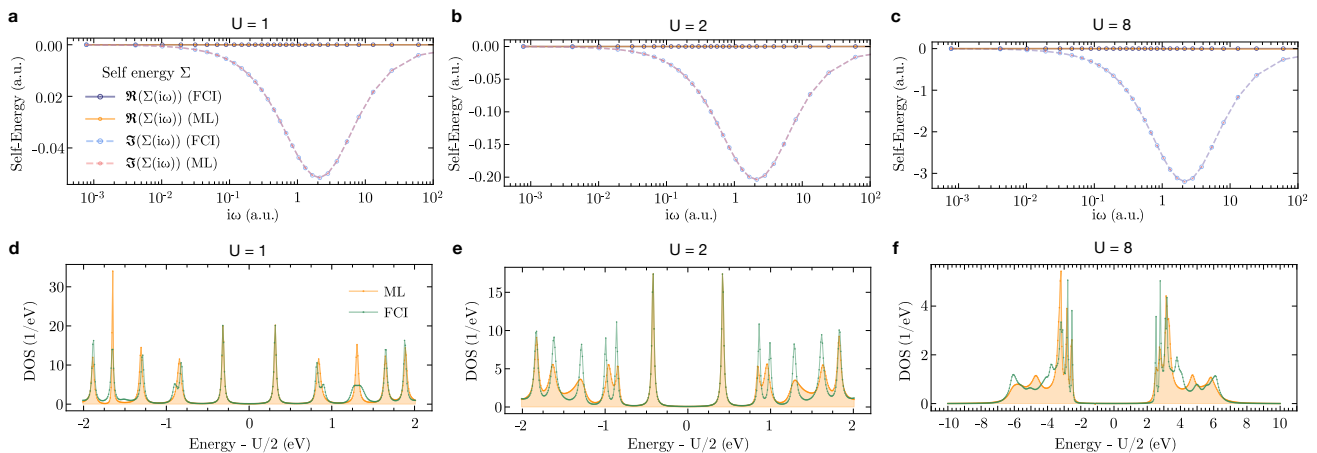


FIG. 2. Self-energy and DOS for unseen test data of a Hubbard model with nearest-neighbor interactions $t = 1$. (a)-(c) Local self-energy on leftmost site $\Sigma_{1,1}(i\omega)$ versus frequency for $U = 1$, $U = 2$, and $U = 8$, respectively. Machine-learned prediction (ML, orange, small circles) versus exact solution (FCI, blue, large circles). Solid lines: real part. Dashed line: imaginary part. (d)-(f) DOS from FCI (green line) compared to ML prediction (orange filled area) around the Fermi energy $E_F = U/2$.

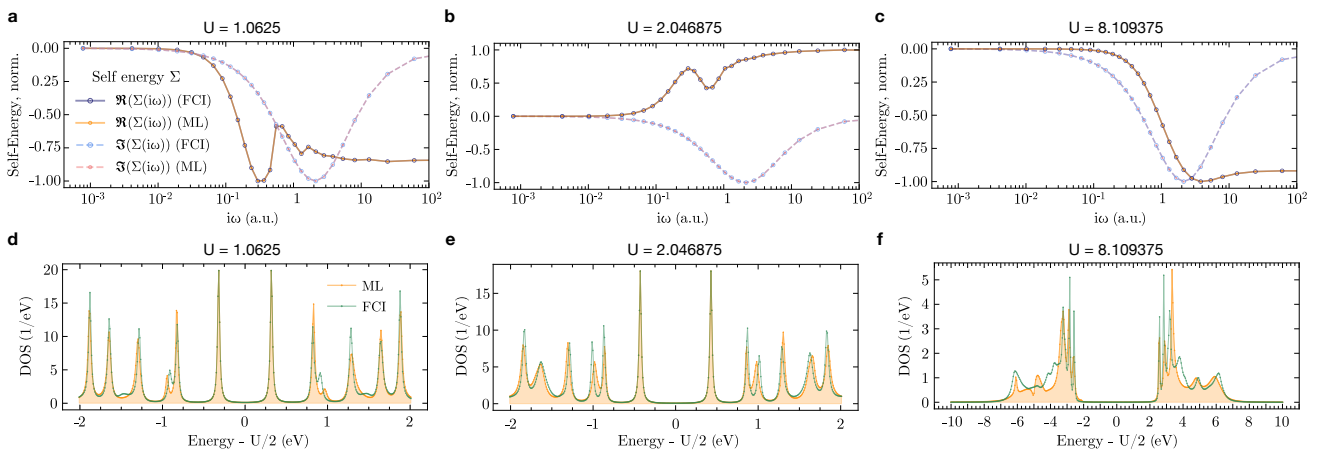


FIG. 3. Same as fig. 2, but for training data. (a)-(c) Local self-energy $\Sigma_{1,1}(i\omega)$ in normalized units versus frequency for $U = 1.0625$, $U = 2.046875$, and $U = 8.109375$, respectively, and (d)-(f) DOS around the Fermi energy for the same U -values.

as a function of energy is symmetric w.r.t. the Fermi level at $U/2$, which could be used to enhance the accuracy of the A.C., for example, by only predicting a subset of the energies. Another way of improving the results is by increasing the amount of training data, which we expect[20] will lead to better results, a direction we did not pursue due to the computational cost of the FCI calculations.

B. Long-Range Interactions

1. Test Data

A current challenge with most computational methods is capturing long-range interactions. In the following, we focus on a Hubbard model with nearest-neighbor hopping $t = 1$ and long-range hopping terms $t' = 0.25$ and $t'' = 0.1$. In fig. 5(a) and (b), we present the exact and predicted DOS for unseen test data with $U = 1$ and $U = 6$, respectively. Note that the Fermi level is shifted from $U/2$. The predicted DOS is close to the exact result, and the ML model captures both the

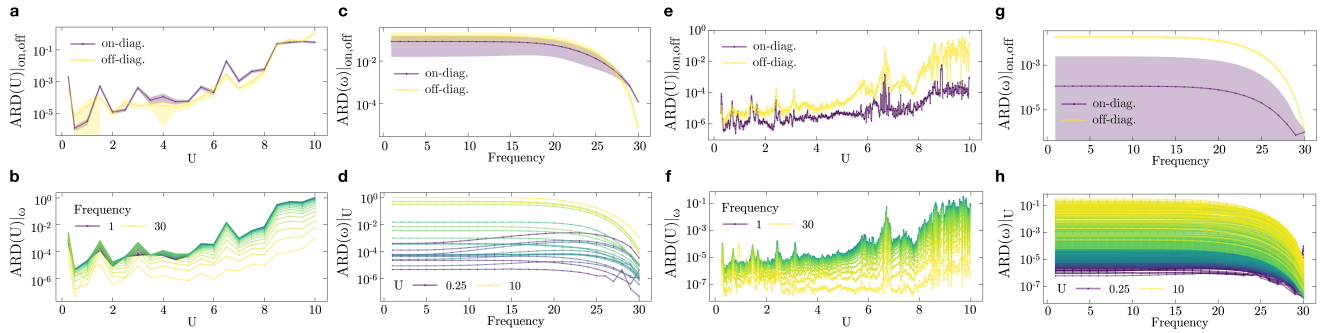


FIG. 4. Overview of absolute relative difference (ARD) between exact and ML-predicted self-energy of the Hubbard model with nearest-neighbor hopping $t = 1$. (a)-(d) show results for test data, and (e)-(h) for training data. (a) $\text{ARD}(U)|_{\text{on,off}}$ for all on- and off-diagonal matrix elements, showing that systems with large U can be predicted less accurately. (b) $\text{ARD}(U)|_{\omega}$ for individual frequencies from smallest ω_1 (purple) to largest ω_{30} (yellow) shows reduced accuracy at small frequencies. (c) $\text{ARD}(\omega)|_{\text{on,off}}$ as a function of frequency over all U shows nearly constant error across most frequencies. (d) $\text{ARD}(\omega)|_U$ for different interaction strengths from $U = 0.25$ (purple) to $U = 10$ (yellow) as a function of frequency index. Note that no error bars are plotted for the bottom plots. (e)-(h) Corresponding quantities for the training data.

position and relative height of most peaks. The predicted local self-energy on the first site shows slight deviations from the exact solution for frequencies around $i\omega \approx 1$ for $U = 6$, see fig. 5(c). The same data is presented in fig. 5(d)-(f) for a system with an additional hopping term $t''' = 0.1$. Note that we use a kernel with six (K_6) instead of three (K_3) Matérn functions for calculations with $t''' \neq 0$. We provide a comprehensive comparison between these kernels in the appendix[52]. Our improved kernel K_6 is able to capture the relationship between features and targets more accurately compared to K_3 for the same system parameters, increasing the accuracy for the case with $t''' \neq 0$.

2. Accuracy of Predictions

In fig. 6, we provide an overview of the ARD for a system with long-range hopping terms $t' = 0.25$, $t'' = 0.1$, and $t''' = 0$. The ARD increases for test data with larger U -values, see fig. 6(a), although less pronounced compared to the trends in fig. 4(a). We achieve relative errors between 10^{-4} and 10^{-2} over a large range of interaction strengths (fig. 6(b)), where the best accuracy is reached at low and intermediate U -values, see also fig. 6(d). The ARD curve in fig. 6(c) is different compared to the case with purely nearest-neighbor interactions in fig. 4(c), which can be explained by a different frequency dependence of $\Sigma(i\omega)$ for systems with long-range interactions. Similarly, we see in fig. 6(d) that the largest ARD occurs at larger frequency values around ω_{20} instead of ω_1 . In fig. 6(e)-(h), we present the same metrics for our training data. The ARD for the off-diagonal matrix elements (yellow) increases with the on-site Coulomb repulsion U (fig. 6(e)), because off-diagonal elements corresponding to long-range interac-

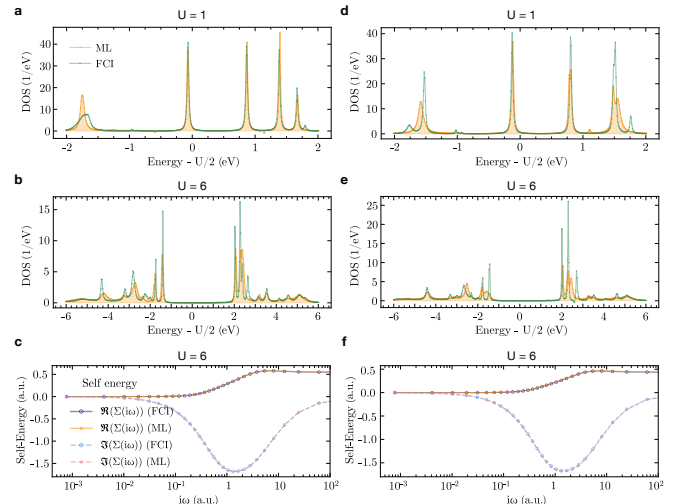


FIG. 5. Test data for a Hubbard model with $t = 1$, $t' = 0.25$, and $t'' = 0.1$. Comparison of ML prediction to FCI for (a) and (b) DOS at $U = 1$ and $U = 6$, respectively, and (c) local self-energy $\Sigma_{1,1}(i\omega)$ versus frequency for $U = 6$. (d) and (e) DOS for a system with additional interaction $t''' = 0.1$ for $U = 1$ and $U = 6$, respectively, and (f) local self-energy for $U = 6$.

tions become more important for systems with larger U . On the other hand, the ARD does not show this trend for on-diagonal terms (purple), which is why training separate models for on- and off-diagonal elements is a useful design choice. For the training data, the relative differences are as low as 10^{-5} and 10^{-8} for small and large frequencies, respectively, indicating near-exact results (fig. 6(f)). This increases our confidence that this ML model can relate mean-field features to the many-body self-energy. We observe that the ARD is less de-

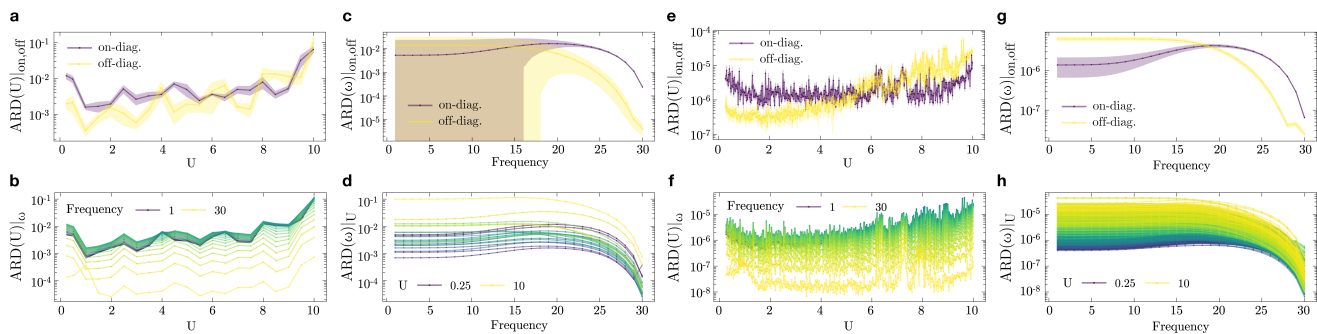


FIG. 6. Same as fig. 4, but for a Hubbard model with long-range interactions $t = 1$, $t' = 0.25$, and $t'' = 0.1$. ARD for (a)-(d) test data and (e)-(h) training data.

pendent on U for systems with long-range interactions, see fig. 6(f) in comparison to fig. 4(f). This is another indication that our method might be particularly well suited for systems with complicated long-range interactions that modify the self-energy function in a favorable way for our ML framework, see also fig. 6(g) in comparison to the nearest-neighbor Hubbard model in fig. 4(g).

In the appendix, we present the same overview for the case with $t''' = 0.1$ [52]. Similar to the previous results, we find an ARD as low as 10^{-3} and 10^{-7} over a large range of U -values for test and training data, respectively.

IV. CONCLUSION

In this work, we demonstrate that an ML framework based on Kernel Ridge Regression (KRR) can learn and predict the imaginary-frequency self-energy function of one-dimensional Hubbard models across a wide range of on-site interaction strengths, including both short- and long-range hopping terms. In all examples, the predicted self-energies exhibit a low absolute relative difference (ARD) compared to the exact results. Using Padé analytic continuation (A.C.), we transform the self-energy calculated on the imaginary frequency axis to the real energy axis, enabling us to predict the density of states (DOS). We attribute the main source of error in the DOS predictions to the A.C. method rather than to the ML model. Counterintuitively, systems with long-range hopping terms are predicted with lower relative errors than nearest-neighbor models, suggesting that our method may be particularly well-suited for real materials with complex interactions. Our findings indicate that the mean-field quantities of the one-dimensional Hubbard model contain sufficient information for a KRR model to reproduce and predict many-body self-energies and capture the signatures of

strong correlations in spectral observables. We show that the highly nonlinear structure of deep neural networks, which makes them challenging to interpret, is not required to capture the spectral features of strongly correlated quantum systems. Instead, our results suggest that simpler ML models such as KRR might be sufficient to learn signatures of strong correlations.

In future work, our ML framework could be extended to predict spectral properties of lattice models with varying electron and hole doping, system sizes, dimensionality, or interaction strengths, possibly by employing a Mixture-of-Experts (MoE) approach. A natural next step is to investigate how well our model generalizes to larger systems or related systems such as the tJ -model. Another open question concerns the connection between one- and two-dimensional lattice models. Our framework may help explore whether two-dimensional correlations can be inferred from one-dimensional systems, possibly advancing the understanding of topological phenomena[53] or superconductivity[54].

ACKNOWLEDGEMENTS

I am grateful for the ongoing support from Tianyu Zhu, as well as for fruitful discussions and the hospitality of his group. I would like to thank Uli Schollwöck, Chris Roth, Jason Kaye, and Andrew J. Millis for their helpful comments on this manuscript. I thank Christian Venturella, Christopher Hillenbrand, and Jiachen Li for helpful discussions and support with the MLGF library. I am grateful for the hospitality of the Center for Computational Quantum Physics at the Flatiron Institute. The Flatiron Institute is a division of the Simons Foundation. I acknowledge funding from the German Academic Scholarship Foundation and the Swiss Study Foundation.

-
- [1] Christian Venturella, Christopher Hillenbrand, Jiachen Li, and Tianyu Zhu. Machine learning many-body green's functions for molecular excitation spectra. *Journal of Chemical Theory and Computation*, 20(1):143–154, 2024. PMID: 38150268.
- [2] Antoine Georges, Gabriel Kotliar, Werner Krauth, and Marcelo J. Rozenberg. Dynamical mean-field theory of strongly correlated fermion systems and the limit of infinite dimensions. *Rev. Mod. Phys.*, 68:13–125, Jan 1996.
- [3] Gabriel Kotliar and Dieter Vollhardt. Strongly correlated materials: Insights from dynamical mean-field theory. *Physics Today*, 57(3):53–59, 03 2004.
- [4] G. Kotliar, S. Y. Savrasov, K. Haule, V. S. Oudovenko, O. Parcollet, and C. A. Marianetti. Electronic structure calculations with dynamical mean-field theory. *Rev. Mod. Phys.*, 78:865–951, Aug 2006.
- [5] Sudeshna Sen, Patrick J. Wong, and Andrew K. Mitchell. The mott transition as a topological phase transition. *Phys. Rev. B*, 102:081110, Aug 2020.
- [6] J. C. Slater. A simplification of the hartree-fock method. *Phys. Rev.*, 81:385–390, Feb 1951.
- [7] Volker Bach, Elliott H. Lieb, and Jan Philip Solovej. Generalized hartree-fock theory and the hubbard model. *Journal of Statistical Physics*, 76(1):3–89, 1994.
- [8] W. Kohn and L. J. Sham. Self-consistent equations including exchange and correlation effects. *Phys. Rev.*, 140:A1133–A1138, Nov 1965.
- [9] Aron J. Cohen, Paula Mori-Sánchez, and Weitao Yang. Challenges for density functional theory. *Chemical Reviews*, 112(1):289–320, 01 2012.
- [10] John E. Coulter, Efstratios Manousakis, and Adam Gali. Limitations of the hybrid functional approach to electronic structure of transition metal oxides. *Phys. Rev. B*, 88:041107, Jul 2013.
- [11] George H. Booth and Garnet Kin-Lic Chan. Spectral functions of strongly correlated extended systems via an exact quantum embedding. *Phys. Rev. B*, 91:155107, Apr 2015.
- [12] Tianyu Zhu, Carlos A. Jiménez-Hoyos, James McClain, Timothy C. Berkelbach, and Garnet Kin-Lic Chan. Coupled-cluster impurity solvers for dynamical mean-field theory. *Phys. Rev. B*, 100:115154, Sep 2019.
- [13] Dorothea Golze, Marc Dvorak, and Patrick Rinke. The gw compendium: A practical guide to theoretical photoemission spectroscopy. *Frontiers in Chemistry*, Volume 7 - 2019, 2019.
- [14] Marcel Nooijen and Jaap G. Snijders. Coupled cluster approach to the single-particle green's function. *International Journal of Quantum Chemistry*, 44(S26):55–83, 1992.
- [15] Rodney J. Bartlett and Monika Musiał. Coupled-cluster theory in quantum chemistry. *Rev. Mod. Phys.*, 79:291–352, Feb 2007.
- [16] Fabian H. L. Essler, Holger Frahm, Frank Göhmann, Andreas Klümper, and Vladimir E. Korepin. *The One-Dimensional Hubbard Model*. Cambridge University Press, 2005.
- [17] R. Preuss, A. Muramatsu, W. von der Linden, P. Dieterich, F. F. Assaad, and W. Hanke. Spectral properties of the one-dimensional hubbard model. *Phys. Rev. Lett.*, 73:732–735, Aug 1994.
- [18] Hao-Xin Wang, Yi-Ming Wu, Yi-Fan Jiang, and Hong Yao. Spectral properties of a one-dimensional extended hubbard model from bosonization and time-dependent variational principle: Applications to one-dimensional cuprates. *Phys. Rev. B*, 109:045102, Jan 2024.
- [19] Lars Hedin. New method for calculating the one-particle green's function with application to the electron-gas problem. *Phys. Rev.*, 139:A796–A823, Aug 1965.
- [20] Louis-Fran çois Arsenault, Alejandro Lopez-Bezanilla, O. Anatole von Lilienfeld, and Andrew J. Millis. Machine learning for many-body physics: The case of the anderson impurity model. *Phys. Rev. B*, 90:155136, Oct 2014.
- [21] Douglas Hendry and Adrian E. Feiguin. Machine learning approach to dynamical properties of quantum many-body systems. *Phys. Rev. B*, 100:245123, Dec 2019.
- [22] Yusuke Nomura, Andrew S. Darmawan, Youhei Yamaji, and Masatoshi Imada. Restricted boltzmann machine learning for solving strongly correlated quantum systems. *Phys. Rev. B*, 96:205152, Nov 2017.
- [23] James Stokes, Javier Robledo Moreno, Eftychios A. Pnevmatikakis, and Giuseppe Carleo. Phases of two-dimensional spinless lattice fermions with first-quantized deep neural-network quantum states. *Phys. Rev. B*, 102:205122, Nov 2020.
- [24] Yangjun Wu, Chu Guo, Yi Fan, Pengyu Zhou, and Honghui Shang. Nnqs-transformer: an efficient and scalable neural network quantum states approach for ab initio quantum chemistry. In *Proceedings of the International Conference for High Performance Computing, Networking, Storage and Analysis*, SC '23, New York, NY, USA, 2023. Association for Computing Machinery.
- [25] Hannah Lange, Anka Van de Walle, Atiye Abedinnia, and Annabelle Bohrdt. From architectures to applications: a review of neural quantum states. *Quantum Science and Technology*, 9(4):040501, sep 2024.
- [26] Riccardo Rende, Sebastian Goldt, Federico Becca, and Luciano Loris Viteritti. Fine-tuning neural network quantum states. *Phys. Rev. Res.*, 6:043280, Dec 2024.
- [27] Tiago Mendes-Santos, Markus Schmitt, and Markus Heyl. Highly resolved spectral functions of two-dimensional systems with neural quantum states. *Phys. Rev. Lett.*, 131:046501, Jul 2023.
- [28] Maarten Van Damme and Laurens Vanderstraeten. Momentum-resolved time evolution with matrix product states. *Phys. Rev. B*, 105:205130, May 2022.
- [29] Erica J. Sturm, Matthew R. Carbone, Deyu Lu, Andreas Weichselbaum, and Robert M. Konik. Predicting impurity spectral functions using machine learning. *Phys. Rev. B*, 103:245118, Jun 2021.
- [30] Yuanran Zhu, Jia Yin, Cian C Reeves, Chao Yang, and Vojtěch Vlček. Predicting nonequilibrium green's func-

- tion dynamics and photoemission spectra via nonlinear integral operator learning. *Machine Learning: Science and Technology*, 6(1):015027, feb 2025.
- [31] Steven R. White. Density matrix formulation for quantum renormalization groups. *Phys. Rev. Lett.*, 69:2863–2866, Nov 1992.
- [32] Ulrich Schollwöck. The density-matrix renormalization group in the age of matrix product states. *Annals of Physics*, 326(1):96–192, 2011. January 2011 Special Issue.
- [33] C. N. Varney, C.-R. Lee, Z. J. Bai, S. Chiesa, M. Jarrell, and R. T. Scalettar. Quantum monte carlo study of the two-dimensional fermion hubbard model. *Phys. Rev. B*, 80:075116, Aug 2009.
- [34] Giuseppe Carleo and Matthias Troyer. Solving the quantum many-body problem with artificial neural networks. *Science*, 355(6325):602–606, 2017.
- [35] Kenny Choo, Antonio Mezzacapo, and Giuseppe Carleo. Fermionic neural-network states for ab-initio electronic structure. *Nature Communications*, 11(1):2368, 2020.
- [36] Kenny Choo, Giuseppe Carleo, Nicolas Regnault, and Titus Neupert. Symmetries and many-body excitations with neural-network quantum states. *Phys. Rev. Lett.*, 121:167204, Oct 2018.
- [37] E.M. Stoudenmire and Steven R. White. Studying two-dimensional systems with the density matrix renormalization group. *Annual Review of Condensed Matter Physics*, 3(Volume 3, 2012):111–128, 2012.
- [38] U. Schollwöck. The density-matrix renormalization group. *Rev. Mod. Phys.*, 77:259–315, Apr 2005.
- [39] F. Verstraete, D. Porras, and J. I. Cirac. Density matrix renormalization group and periodic boundary conditions: A quantum information perspective. *Phys. Rev. Lett.*, 93:227205, Nov 2004.
- [40] E. Y. Loh, J. E. Gubernatis, R. T. Scalettar, S. R. White, D. J. Scalapino, and R. L. Sugar. Sign problem in the numerical simulation of many-electron systems. *Phys. Rev. B*, 41:9301–9307, May 1990.
- [41] Kevin Vu, John C. Snyder, Li Li, Matthias Rupp, Brandon F. Chen, Tarek Khelif, Klaus-Robert Müller, and Kieron Burke. Understanding kernel ridge regression: Common behaviors from simple functions to density functionals. *International Journal of Quantum Chemistry*, 115(16):1115–1128, 2015.
- [42] A.L. Fetter and J.D. Walecka. *Quantum Theory of Many-particle Systems*. Dover Books on Physics. Dover Publications, 2003.
- [43] H. J. Vidberg and J. W. Serene. Solving the eliashberg equations by means ofn-point padéapproximants. *Journal of Low Temperature Physics*, 29(3):179–192, 1977.
- [44] Qiming Sun, Xing Zhang, Samraghi Banerjee, Peng Bao, Marc Barbry, Nick S. Blunt, Nikolay A. Bogdanov, George H. Booth, Jia Chen, Zhi-Hao Cui, Janus J. Erikson, Yang Gao, Sheng Guo, Jan Hermann, Matthew R. Hermes, Kevin Koh, Peter Koval, Susi Lehtola, Zhen-dong Li, Junzi Liu, Narbe Mardirossian, James D. McClain, Mario Motta, Bastien Mussard, Hung Q. Pham, Artem Pulkin, Wirawan Purwanto, Paul J. Robinson, Enrico Ronca, Elvira R. Sayfutyarova, Maximilian Scheurer, Henry F. Schurkus, James E. T. Smith, Chong Sun, Shi-Ning Sun, Shiv Upadhyay, Lucas K. Wagner, Xiao Wang, Alec White, James Daniel Whitfield, Mark J. Williamson, Sebastian Wouters, Jun Yang, Jason M. Yu, Tianyu Zhu, Timothy C. Berkelbach, Sandeep Sharma, Alexander Yu. Sokolov, and Garnet Kin-Lic Chan. Recent developments in the pyscf program package. *The Journal of Chemical Physics*, 153(2):024109, 07 2020.
- [45] Qiming Sun, Timothy C. Berkelbach, Nick S. Blunt, George H. Booth, Sheng Guo, Zhendong Li, Junzi Liu, James D. McClain, Elvira R. Sayfutyarova, Sandeep Sharma, Sebastian Wouters, and Garnet Kin-Lic Chan. Pyscf: the python-based simulations of chemistry framework. *WIREs Computational Molecular Science*, 8(1):e1340, 2018.
- [46] Tianyu Zhu and Garnet Kin-Lic Chan. Ab initio full cell gw + DMFT for correlated materials. *Phys. Rev. X*, 11:021006, Apr 2021.
- [47] Tianyu Zhu, Zhi-Hao Cui, and Garnet Kin-Lic Chan. Efficient formulation of ab initio quantum embedding in periodic systems: Dynamical mean-field theory. *Journal of Chemical Theory and Computation*, 16(1):141–153, 01 2020.
- [48] Tianyu Zhu and Garnet Kin-Lic Chan. All-electron gaussian-based g_0w_0 for valence and core excitation energies of periodic systems. *Journal of Chemical Theory and Computation*, 17(2):727–741, 2021. PMID: 33397095.
- [49] Carl Edward Rasmussen and Christopher K. I. Williams. *Gaussian Processes for Machine Learning*. The MIT Press, 11 2005.
- [50] F. Pedregosa, G. Varoquaux, A. Gramfort, V. Michel, B. Thirion, O. Grisel, M. Blondel, P. Prettenhofer, R. Weiss, V. Dubourg, J. Vanderplas, A. Passos, D. Cournapeau, M. Brucher, M. Perrot, and E. Duchesnay. Scikit-learn: Machine learning in Python. *Journal of Machine Learning Research*, 12:2825–2830, 2011.
- [51] Welling Max. Kernel ridge regression, max welling’s classnotes in machine learning., 2013.
- [52] See Supplemental Material at [URL will be inserted by publisher] for an overview of the DOS obtained from HF and first-order G_0W_0 calculations and many-body predictions, a comparison of different kernel functions, and an overview of the ARD for long-range hopping terms with $t''' = 0.1$.
- [53] Wei Wu, Mathias S. Scheurer, Shubhayu Chatterjee, Subir Sachdev, Antoine Georges, and Michel Ferrero. Pseudogap and fermi-surface topology in the two-dimensional hubbard model. *Phys. Rev. X*, 8:021048, May 2018.
- [54] Xin-Zhong Yan. Superconductivity in the quasi-two-dimensional hubbard model. *Phys. Rev. B*, 71:104520, Mar 2005.

Appendix A

1. Hartree-Fock Convergence

In the following, we present our procedure to find the Hartree-Fock (HF) ground state of the $L = 10$ Hubbard model. In order to reach convergence, we use an iterative approach with an initial density matrix guess for all calculations over the range of U -values with N electrons:

$$\rho_{\text{init}} = \frac{1}{2}(\rho_{\text{alt}} + \rho_{\text{prev}}) \quad (\text{A1})$$

where ρ_{prev} is the converged density matrix of the next-smallest U -value, and $\rho_{\text{prev}} = \rho_{\text{alt}}$ for the smallest U -value. $\rho_{\text{alt}} = (\rho_{\text{alt}}^{\uparrow}, \rho_{\text{alt}}^{\downarrow})$ consists of $\rho_{\text{alt}}^{\uparrow} = \text{diag}(0.7, 0.3, \dots)$ and $\rho_{\text{alt}}^{\downarrow} = \text{diag}(0.3, 0.7, \dots)$ such that in total N elements of ρ_{alt} are nonzero. If this calculation does not converge, we first use only the previous density matrix $\rho_{\text{init}} = \rho_{\text{prev}}$ and then add a random initial guess:

$$\rho_{\text{init}} = a \cdot \rho_{\text{random}} + b \cdot \rho_{\text{prev}} \quad (\text{A2})$$

with

$$\rho_{\text{random}} = (\text{diag}(x_1, \dots, x_L), \text{diag}(x'_1, \dots, x'_L)) \quad (\text{A3})$$

where $\{x_i\}_{i=1, \dots, L}, \{x'_i\}_{i=1, \dots, L}$ are independent random numbers. We define a maximum number of iterations M and determine the mixture of the previous density matrix ρ_{prev} and the random density matrix ρ_{random} in the j -th round through

$$r = \frac{M - 2 - (j - 2)}{M - 2}, \quad a = 1 - r, \quad b = r. \quad (\text{A4})$$

For the $M/2$ -th round, we add random off-diagonal elements:

$$\rho_{\text{random}} = (X, X') \quad (\text{A5})$$

where $\{X_{ij}\}_{i,j=1, \dots, L}, \{X'_{i,j}\}_{i,j=1, \dots, L}$ are random matrix elements. This procedure often converges within the first iteration, and we typically need less than 10 iterations for most parameters.

2. Machine-Learning Method

One may argue that spectral functions can easily be obtained from computationally less expensive methods than FCI, hence making the ML approach redundant. While this is certainly the case for weakly interacting systems such as molecules, we show in fig. A.7(a) that the DOS is different even at $U = 1$ if obtained only from mean-field calculations (purple) compared to our ML method which incorporates the many-body interactions (orange). In the former case, we see that the quasiparticle peaks are shifted towards the Fermi level. We also compare a calculation which uses the first-order G_0W_0 self-energy combined with the mean-field Green's function G_0 via Dyson's equation (turquoise). This data shows that we are not providing the many-body self-energy to our ML model by using the G_0W_0 self-energy Σ_{GW} in our feature vector. In fig. A.7(b), (c), and (d), we show the same data for $U = 2$, $U = 4$, and $U = 8$, respectively. We can clearly see that the DOS is not accurate at all if we would only rely on a mean-field framework.

The ML-GF is obtained by predicting the self-energy on the imaginary frequency axis, combining it with the HF-GF to obtain the predicted Green's function on the imaginary axis, and then using A.C. to obtain the ML-GF from which we can calculate the DOS as a function of energy. We found that reversing the steps, i.e., first performing A.C. and then using Dyson's equation, consistently led to noisier results. We also performed calculations with different linear combinations of Laplacian and Gaussian kernels, as well as combinations of these with Matérn functions, but we did not find consistent trends to further increase accuracy.

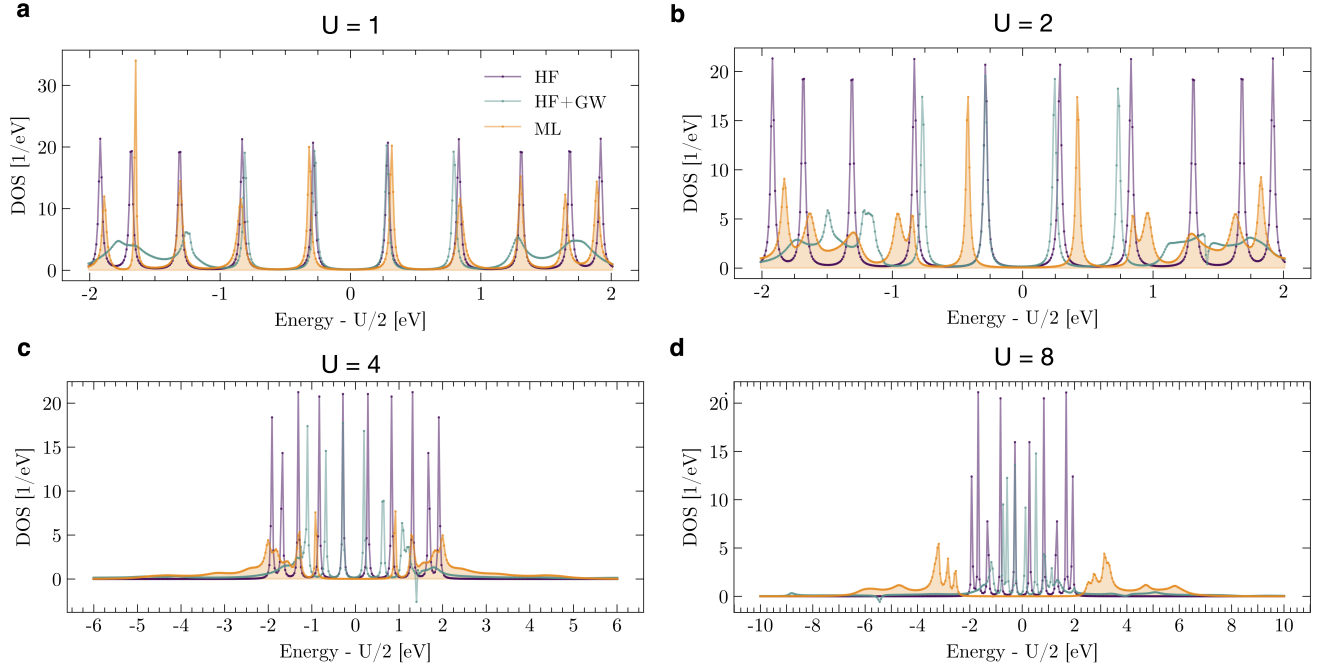


FIG. A.7. Difference in DOS of a nearest-neighbor Hubbard model between the mean-field Green's function (HF, purple) and HF-GF with self-energy from first order GW -calculations (HF + GW, turquoise) in comparison to the predicted Green's function (ML, orange) for different Coulomb repulsions: (a) $U = 1$. (b) $U = 2$. (c) $U = 4$. (d) $U = 8$.

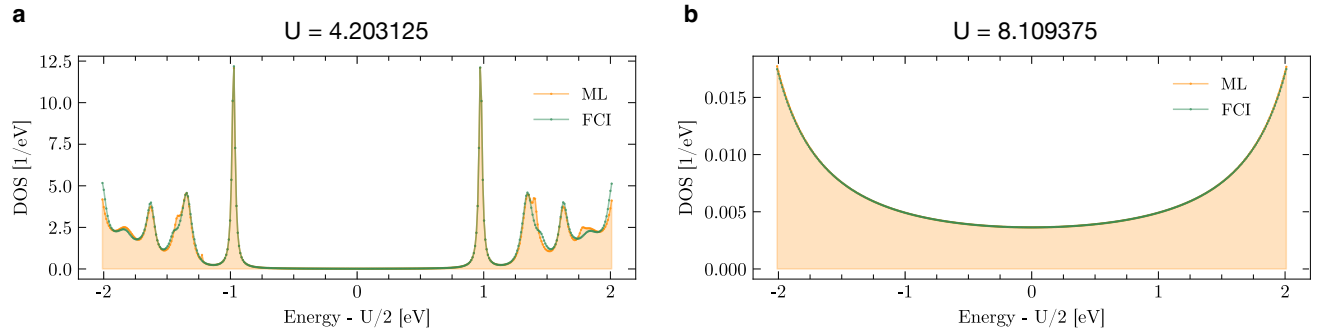


FIG. A.8. DOS of a nearest-neighbor Hubbard model. Comparison of prediction (ML, orange) and exact solution (FCI, green) for training data with (a) $U = 4.203125$ and (b) $U = 8.109375$.

3. Accuracy of Machine-Learning Predictions

In fig. A.8, we show that the ML predictions of the DOS for (a) $U \approx 4$ and (b) $U \approx 8$ align well with the exact solution close to the Fermi edge, while the main deviations occur far away from it.

Our ML framework reproduces training data with high accuracy, both for nearest-neighbor Hubbard models and for Hubbard models with long-range hopping terms. In fig. A.9, we present the same overview of the ARD for the case with $t = 1$, $t' = 0.25$, $t'' = 0.1$, and $t''' = 0.1$, including test data, see fig. A.9(a)-(d), and training data in fig. A.9(e)-(h). Note that we used a kernel with six Matérn functions to achieve high accuracy. For the test data, we find a similar ARD compared to the model with $t''' = 0$, see fig. A.9(a). However, the training data reveals that this system can be learned with slightly higher precision. The highest ARD in fig. A.9(e) is around $2 \cdot 10^{-5}$, while we find approximately $7 \cdot 10^{-5}$ for $t''' = 0$. More remarkably, we find a large difference between the Hubbard model with nearest-neighbor interactions $t = 1$ and the case with additional hopping terms t' , t'' and t''' , see fig. A.9(e). In the former case, we find ARD values between 10^{-6} and 10^{-4} for on-diagonal elements and

10^{-6} and 10^{-1} for off-diagonal elements. On the other hand, the latter model with long-range terms leads to more accurate predictions with ARD values between 10^{-7} and 10^{-5} for both on- and off-diagonal elements.

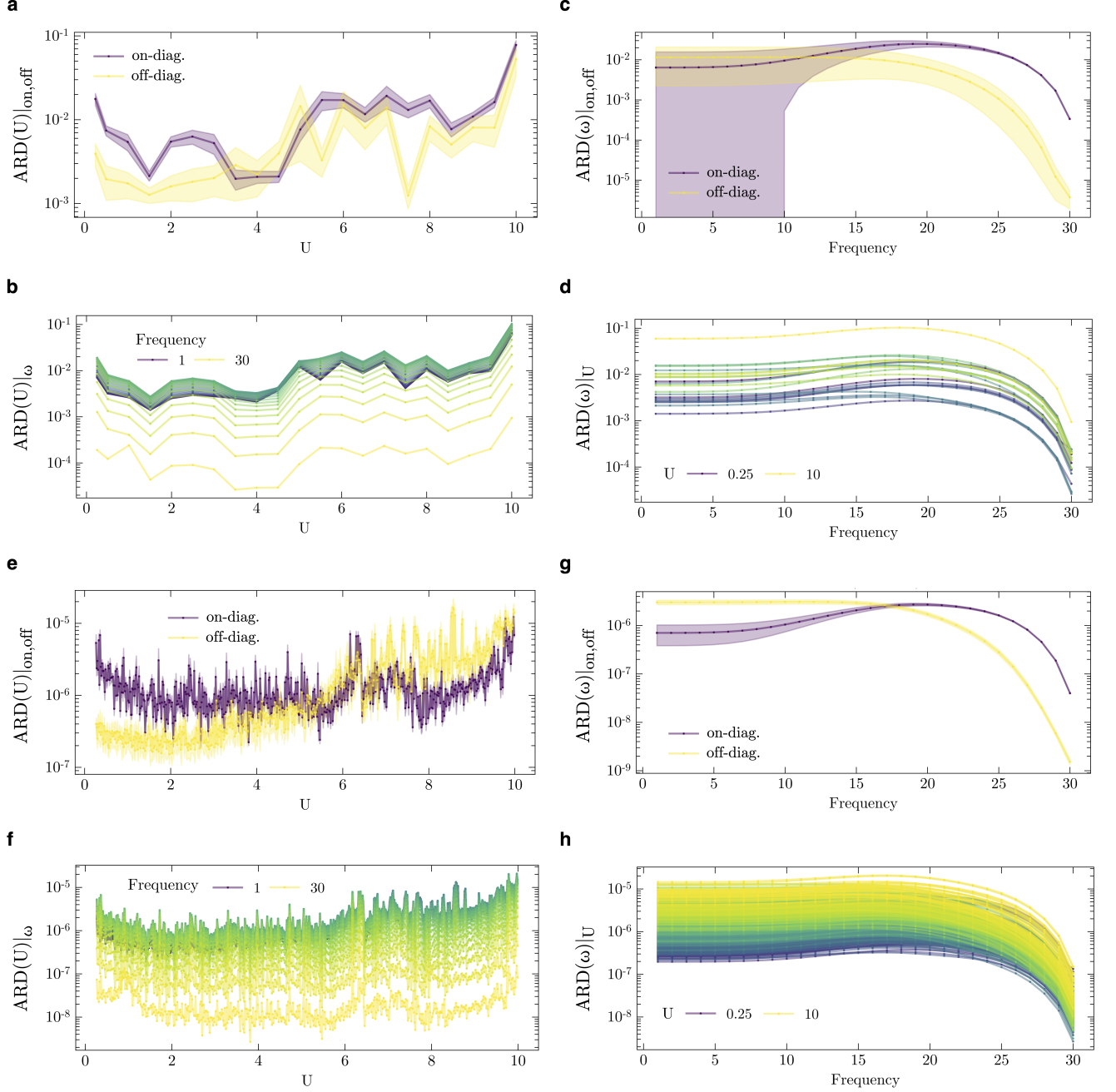


FIG. A.9. Overview of ARD between exact and predicted self-energy for a Hubbard model with long-range interactions $t' = 0.25$, $t'' = 0.1$, $t''' = 0.1$, and with kernel K_6 . ARD for (a)-(d) test data and (e)-(h) training data.

In the following, we show that these self-energy predictions also lead to an accurate DOS. In fig. A.10, we present the ML prediction for training data (orange area) and the exact FCI solution (green line) for a Hubbard model with second ($t' = 0.25$) and third ($t'' = 0.1$) neighbor hopping terms and Coulomb repulsions close to $U \approx 1$, $U \approx 2$, $U \approx 4$, and $U \approx 8$, see fig. A.10(a)-(d), respectively. In fig. A.11, we present the DOS prediction for a Hubbard model which also has an additional hopping $t''' = 0.1$ for the same values of $U \approx 1$, $U \approx 2$, $U \approx 4$, and

$U \approx 8$. In this case, we use a kernel with six Matérn functions (K_6) instead of three. Even for large $U = 8.203125$, the model captures the many-body peaks and their approximate density around ± 7 eV from $E - E_F$. Note that the Fermi level is different from the nearest-neighbor case $E_F = U/2$.

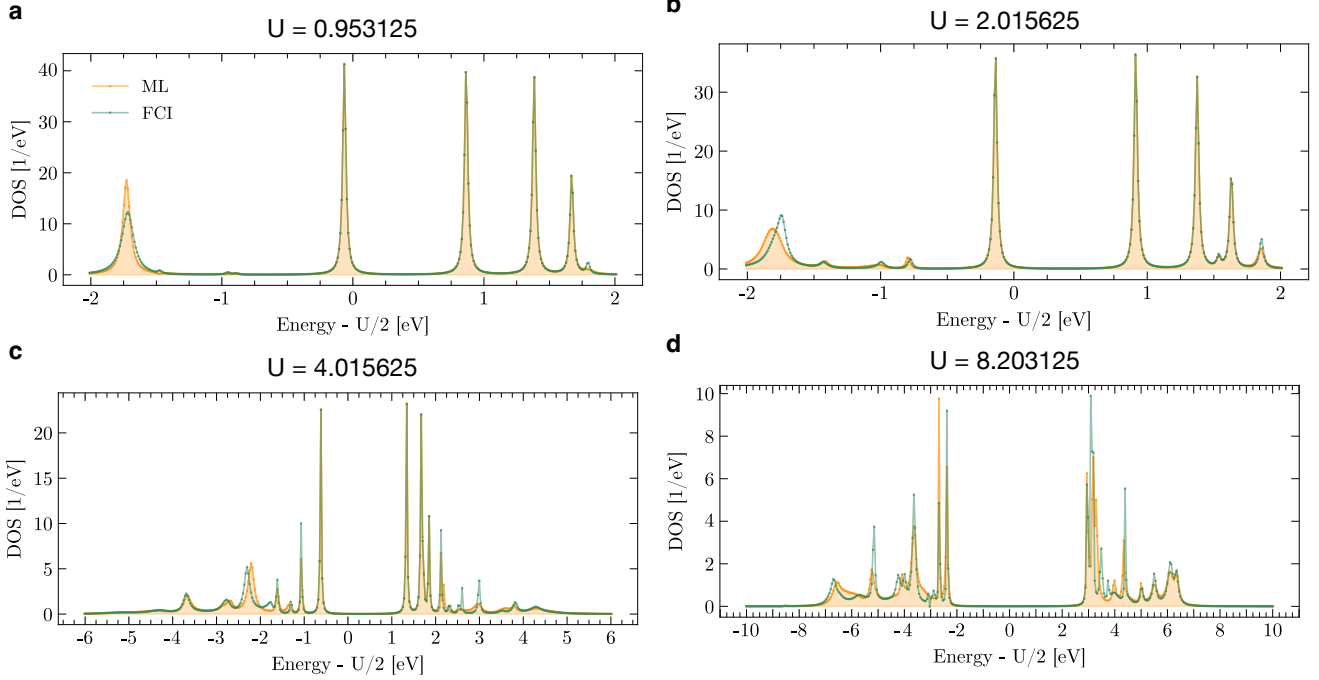


FIG. A.10. DOS of a Hubbard model with long-range hopping terms $t = 1$, $t' = 0.25$, and $t'' = 0.1$. Comparison of ML prediction (orange) and FCI (green) for training data with different Coulomb repulsions (a) $U = 0.953125$, (b) $U = 2.015625$, (c) $U = 4.015625$, and (d) $U = 8.203125$.

4. Comparison of Kernel Functions

In fig. A.12, we present the ARD of our self-energy predictions for unseen test data for a Hubbard model with long-range hopping terms $t' = 0.25$, $t'' = 0.1$ and (a)-(d) $t''' = 0$ as well as (e)-(h) $t''' = 0.1$. We compare the ARD for on- and off-diagonal elements as a function of U -value and frequency in fig. A.12(a) and (b), respectively, with the same metric in fig. A.12(c)-(d), where we use six instead of three Matérn functions in our kernel. We observe that there is no noticeable difference between these two calculations, indicating that three Matérn functions are sufficient to capture all important relationships between the features and the self-energy target for the Hubbard model with $t''' = 0$. On the other hand, we can see from fig. A.12(e) and (f) compared to fig. A.12(g) and (h), respectively, that the accuracy increases significantly in the Hubbard model with $t''' \neq 0$ when using a kernel with six Matérn functions. This includes both the standard deviation, visualized as the shaded area, as well as the ARD value itself. We want to emphasize the first frequency index ω_1 has a significantly higher ARD compared to all other frequency values when using only three Matérn function, see fig. A.12(f), which can be improved by using six Matérn functions, as shown in fig. A.12(h).

The same increase in prediction accuracy can also be observed for training data, see fig. A.13(a)-(d) for $t''' = 0$ and (e)-(h) for $t''' = 0.1$. There is only a slight increase in accuracy between three and six Matérn functions for $t''' = 0$, see fig. A.13(a) versus (c) and also (b) versus (d). For the Hubbard model with $t''' = 0.1$, we observe a difference on the first frequency index ω_1 , see fig. A.13(f) compared to (h). In fig. A.13(e)-(f) versus (g)-(h), respectively, we observe that using more Matérn functions solves this issue, leading to a lower ARD.

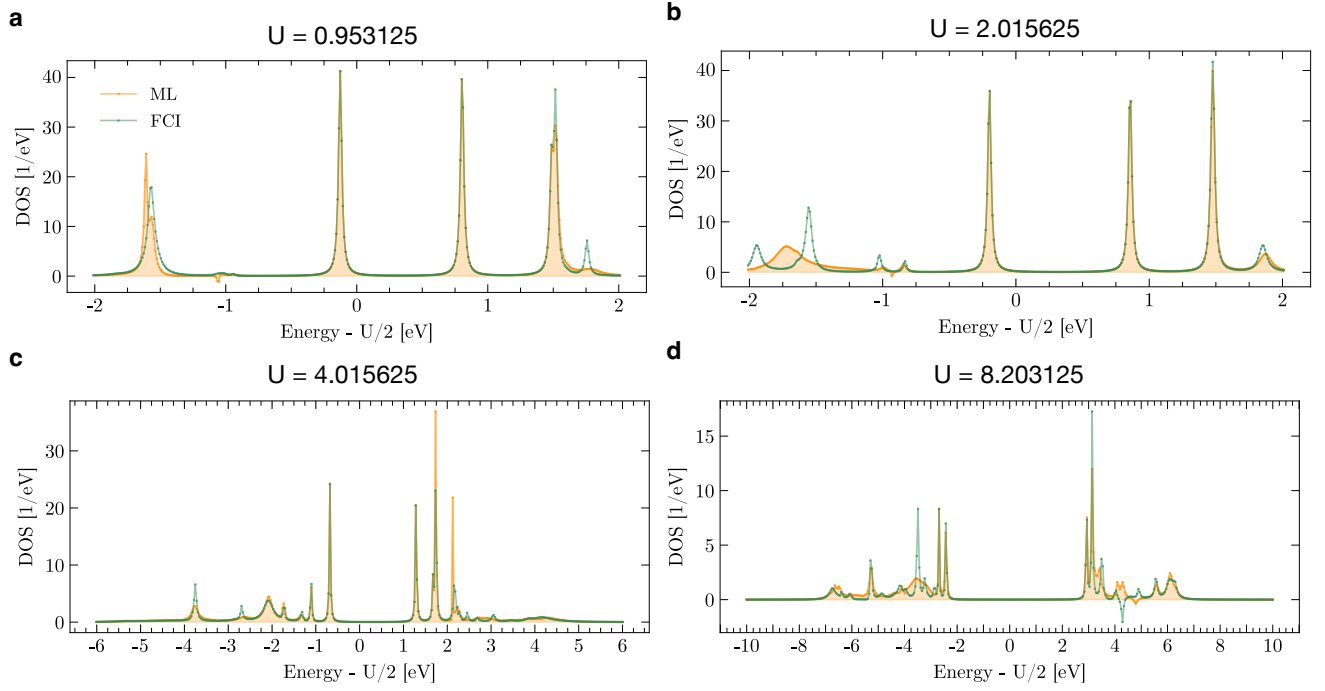


FIG. A.11. Same as figure A.10, but for training data of a Hubbard model with long-range hopping $t = 1$, $t' = 0.25$, $t'' = 0.1$, and $t''' = 0.1$.

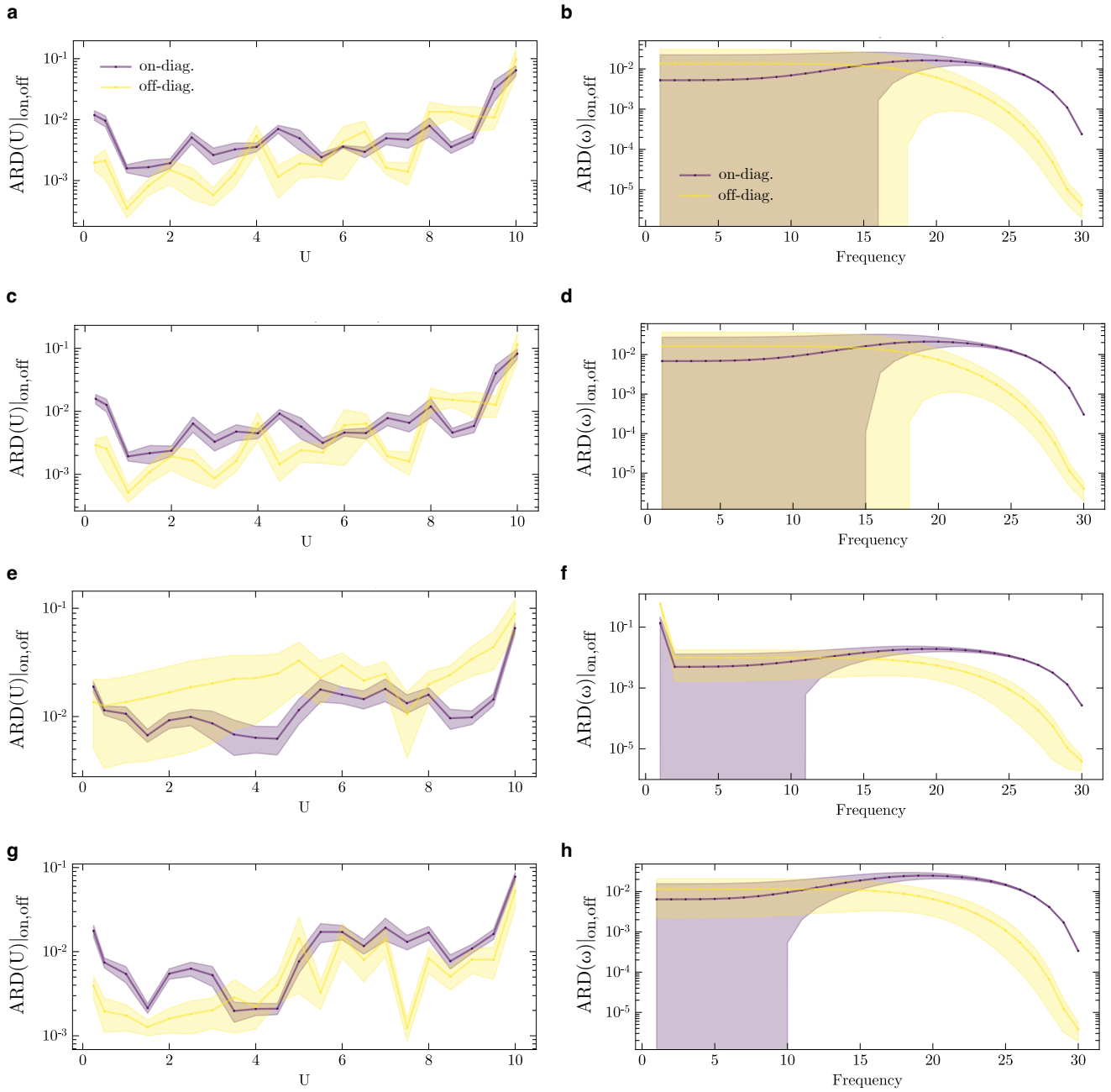


FIG. A.12. ARD for test data of a Hubbard model with long-range hopping terms $t = 1$, $t' = 0.25$, $t'' = 0.1$ and (a)-(d) $t''' = 0$ or (e)-(h) $t''' = 0.1$. We compare a kernel with (a)-(b) three Matern functions K_3 to (c)-(d) six Matern function K_6 for $t''' = 0$. Left column: ARD for all on- (purple line) and off-diagonal (yellow line) matrix elements for different Coulomb interactions U . Right column: ARD as a function of frequency. Shaded areas indicate the standard deviation over all matrix elements of different frequencies (left) or U -values (right). (e)-(h) Same calculation for $t''' = 0.1$ with kernels (e)-(f) K_3 and (g)-(h) K_6 .

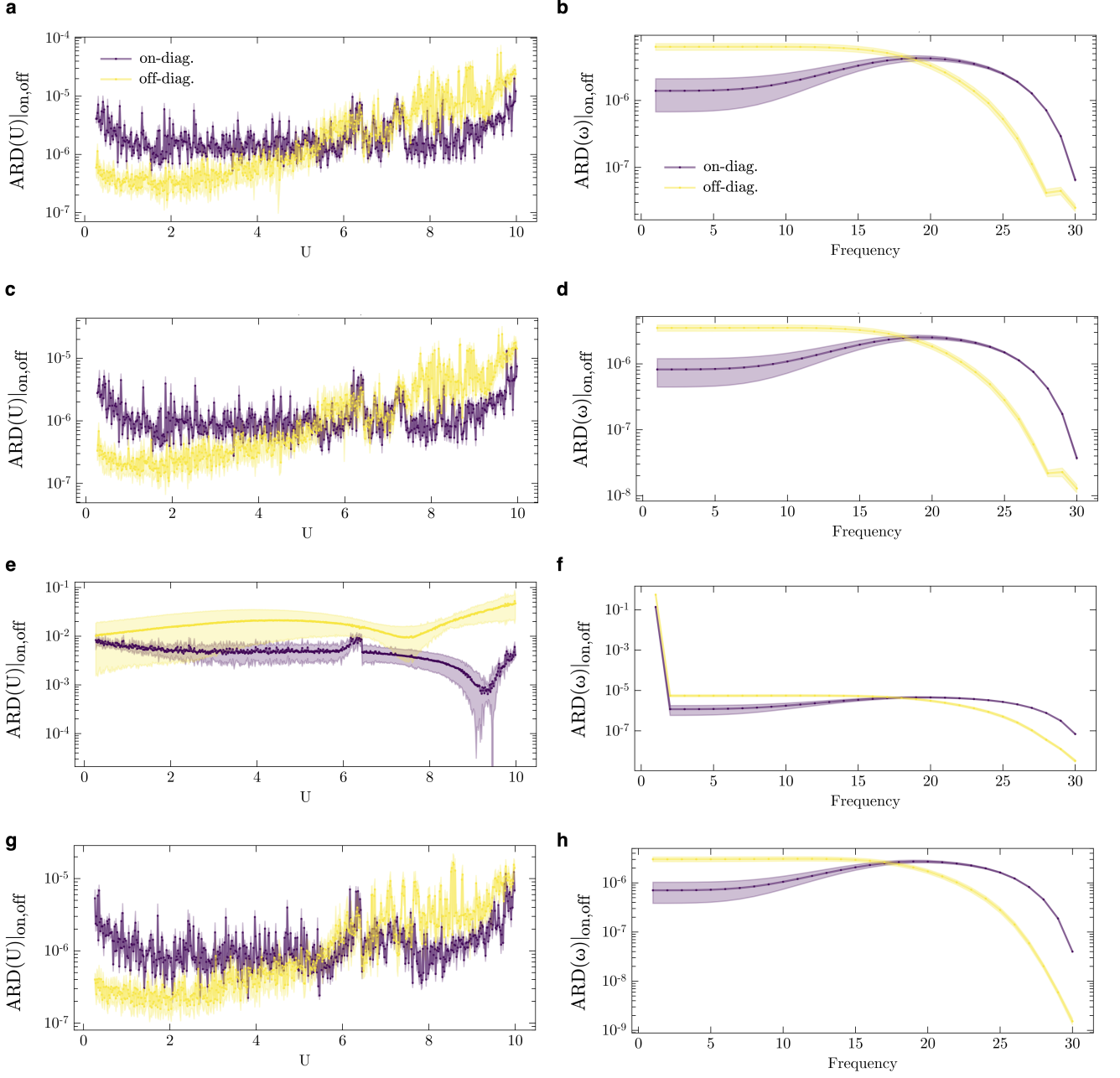


FIG. A.13. Same as fig. A.12, but for training data of a Hubbard model with $t = 1$, $t' = 0.25$, $t'' = 0.1$ and (a)-(d) $t''' = 0$ or (e)-(h) $t''' = 0.1$. Comparison of (a)-(b) and (e)-(f) three Matérn functions K_3 to (c)-(d) and (g)-(h) six Matérn functions K_6 .